Weldability of Additively Manufactured Austenitic Stainless Steels

Increased ductility dip cracking susceptibility of laser powder bed fusion 316L related to primary solidification mode and impurity element segregation

BY O. DENONNO, R. HAMLIN, S. TATE, AND J. KLEMM-TOOLE

Abstract

Additive manufacturing (AM) can enable faster, lower-cost production of power generation components. However, implementation of AM parts into service requires welding to other components, and the weldability of AM alloys is not well characterized. On-cooling hot ductility testing was performed between 1000°C and 1300°C on gas metal arc directed energy deposition (GMA-DED), laser powder bed fusion (L-PBF), and wrought 316-series stainless steels to evaluate weldability and ductility dip cracking (DDC) susceptibility of AM austenitic stainless steels. The results were analyzed with respect to variations in dynamic recrystallization, absorbed energy, and fracture mechanism. Single and multipass autogenous gas tungsten arc welds were performed on GMA-DED, L-PBF, and wrought plates to correlate hot ductility behavior with DDC susceptibility in welded specimens. GMA-DED 316(L/H/LSi) exhibited good hot ductility regardless of post-build heat treatment, while L-PBF 316L exhibited reduced ductility across all conditions. L-PBF 316L also exhibited lower absorbed energy, which correlated with reduced hot ductility and intergranular fracture, whereas the GMA-DED and wrought conditions exhibited greater absorbed energy and ductile fracture. The reduced weldability of L-PBF 316L is suggested to be associated with grain boundary embrittlement from impurity elements segregation during primary austenite solidification. Heat-affected zone microcracking was observed in the GTAW welds of L-PBF 316L, confirming susceptibility to DDC and supporting the correlation between reduced hot ductility and weldability issues.

Keywords

- Weldability
- Ductility Dip Cracking
- Austenitic Stainless Steels
- Gas Metal Arc Additive Directed Energy Deposition
- Laser Powder Bed Fusion

Introduction

Additive manufacturing (AM) processes such as gas metal arc directed energy deposition (GMA-DED) and laser powder bed fusion (L-PBF) offer fabrication pathways that can lead to drastic cost and time savings within the power generation sector. The L-PBF process enables the production of small-scale, near-net shape components with complex geometries, minimizing machining time and material waste (Ref. 1). The GMA-DED process produces larger-scale parts, such as valves, fittings, and reactor internals, at shorter lead times than traditional manufacturing methods, such as forgings and castings (Ref. 2). AM provides a fast and flexible fabrication method for replacement component production, potentially limiting costly plant downtime. However, integration of AM components in service environments will require welding to both AM and conventionally manufactured parts, highlighting the need to understand the weldability of AM austenitic stainless steels.

Austenitic alloys, such as stainless steel and nickel-based superalloys, which are conventionally considered ductile, are observed to experience a distinct reduction in ductility between 0.6 and 0.9 of their solidus temperature (T_s) (Refs. 3–8). This reduction in ductility is attributed to an elevated temperature solid-state cracking mechanism known as ductility dip cracking (DDC). DDC was observed during high temperature deformation processes, such as the continuous casting of steels, where it led to transverse cracking issues (Refs. 5, 9). It has also been reported in multipass welds, where reheating of previous weld layers between 0.6 and 0.9 T_s results

https://doi.org/10.29391/2026.105.024

in intergranular cracking (Refs. 3, 6, 7, 10, 11). Given the similarities between multipass welds and AM components, DDC is a potential concern for austenitic AM alloys.

The mechanism responsible for DDC is still unclear and likely multifaceted. DDC has been associated with factors such as precipitation-induced cracking, grain boundary sliding, and grain boundary embrittlement (Refs. 6, 12). DDC susceptibility is commonly characterized by a ductility trough in a reduction in area (%RA) versus temperature curve. The ductility minimum is typically observed at intermediate temperatures between approximately 0.5 times the homologous temperature and just below the solidus, and is often associated with the onset of grain boundary sliding (Refs. 6, 8). Grain boundary sliding is thought to occur as a strain accommodation mechanism to relieve external welding stresses and to lead to void formation and eventual intergranular cracking (Refs. 6, 10, 12, 13). As the temperature approaches the solidus, ductility is often recovered through dynamic recrystallization (Refs. 4, 5, 8, 12, 14).

Mintz et al. observed a ductility trough in coarse-grained austenitic stainless steel, attributed to grain boundary sliding. In their work, the heat treatment to produce the coarse-grain microstructure resulted in the growth of grain boundary carbides, which were suggested to exacerbate void formation during grain boundary sliding and suppress dynamic recrystallization (Ref. 9). In contrast, the fine-grained austenitic stainless steel did not exhibit a ductility trough, consistent with general observations that DDC is not typically reported in wrought 316 alloys or weldments. Young et al. associated DDC of Ni-Cr alloys with precipitate-induced cracking, where alloys with increased Cr-carbide precipitation saw increased DDC susceptibility due to the generation of local grain boundary stresses from the lattice misfit of the partially coherent carbides (Ref. 15). Conversely, Nissley et al. and Ramirez et al. concluded that precipitates can improve DDC resistance in Ni-based weld metal by pinning grain boundaries and forming tortuous boundaries that inhibit grain boundary sliding (Refs. 10, 12). For low-carbon, solution-annealed 300-series austenitic stainless steels (e.g., 316L), minimal carbide precipitation is expected, suggesting that alternative mechanisms may dominate DDC susceptibility.

Grain boundary embrittlement due to sulfur and phosphorus segregation has also been reported to influence DDC susceptibility. Arata et al. showed that increasing phosphorus levels in Type 310 stainless steel increased DDC susceptibility. Although, even with low levels of phosphorus and sulfur in Type 310, Type 304 displayed higher DDC resistance, which was attributed to primary δ-ferrite solidification compared to primary austenite solidification for Type 310 (Ref. 16). In the development of the strain-to-fracture test, Nissley et al. also found that Type 304 exhibited greater resistance to DDC than Type 310 and several Ni-based alloys. The greater resistance of 304 was associated with the formation of tortuous grain boundaries due to the pinning effect of δ-ferrite, which was not present in any of the other single-phase alloys tested (Ref. 8). Li et al. reported that reduced impurity levels for Type 308 welds were more effective in minimizing heat-affected zone (HAZ) cracking than the presence of δ-ferrite (Ref. 17). Nishimoto et al. observed increased DDC susceptibility in Alloy 690 weld metal with increasing levels of sulfur and phosphorus. DDC susceptibility was reduced with small additions of lanthanum to the filler, which has a high affinity for sulfur and phosphorus (Refs. 11, 18, 19). Nishimoto et al. and Mori et al. confirmed elevated sulfur concentration at intergranular fracture surfaces with Auger electron spectroscopy, supporting the conclusion that grain boundary segregation of impurity elements in the reheated weld metal increases DDC susceptibility (Refs. 18, 20).

Currently, there is extremely limited published work investigating the weldability of AM alloys, with no studies on their DDC susceptibility. The objective of this study is to evaluate the weldability and DDC susceptibility of AM austenitic stainless steels through on-cooling hot ductility testing and constrained autogenous gas tungsten arc welds (GTAW). GMA-DED, L-PBF, and wrought 316-series stainless with various post-build heat treatments were tested, and the results are expected to provide key insights regarding the welding of AM components in power generation applications.

Materials and Methods

Material Fabrication

L-PBF 316L cylindrical vertical rods (114.3 mm L × 7.4 mm diameter) and horizontal plates (114.3 mm L × 101.6 mm W × 7.4 mm T) were printed with an EOS M290 using the process parameters listed in Table 1. The as-built L-PBF material was solution annealed at 1040°C for 1 h, followed by a forced air cool. A subset of material remained in the as-built condition for testing. The material was subsequently machined into 0.25 in. diameter × 4 in. long (6.35 mm × 101.6 mm) cylinders for hot ductility testing.

GMA-DED walls were fabricated using a collaborative robot-controlled Fronius TPS 400i gas metal arc welding (GMAW) heat source. A combination of a low heat input cold metal transfer (CMT) and high heat input pulse multicontrol (PMC) synergistic welding lines, called "CMT mix", was used for the fabrication of the GMA-DED builds. A weaving weld strategy was used to produce three-bead-wide walls with 0.045 in. (1.2 mm) diameter 316L, 316H, and 316LSi welding wires. Welding process parameters are also listed in Table 1. The walls were removed from the 304 baseplate and solution annealed at 1040°C for 1 h, followed by a forced air cool. One GMA-DED 316L wall remained in the as-built condition. The GMA-DED walls were machined into hot ductility rods oriented horizontal to the build direction.

Additional heat treatments were performed on machined hot ductility specimens in a vacuum furnace and cooled with argon backfill. As-built L-PBF 316L vertical specimens were recrystallized at 1200°C for 2 h, while solution annealed GMA-DED 316L/LSi specimens were heat treated at 1150°C for 5 h to dissolve δ-ferrite from the microstructure.

Wrought 316L and 316H material was procured as solution annealed plate and machined into identical hot ductility rods. The composition of the L-PBF and GMA-DED builds and wrought stainless steel plates are reported in Table 2. Carbon, sulfur, oxygen, and nitrogen contents were determined using LECO combustion analysis, while all other elements were determined using optical emission spectroscopy (OES).

Table 1 — L-PBF and GMA-DED Processing Parameters

L-PBF Process Parameters					
Laser Power (W)	Laser Speed (mm/s)	Hatch Spacing (μm)	Hatch Rotation Angle	Layer Thickness (μm)	Volumetric Energy Density (J/mm^3)
214	928	100	47°	40	57.70
GMA-DED Process Parameters					
Wire Feed Rate (mm/s)	Travel Speed (mm/s)	Weave Width (mm)	Layer Rotation Angle	Gas Mixture	Gas Flow Rate (L/min)
78	4	4.5	180°	95% Ar + 5% CO_2	15.1

Table 2 — Chemical Composition of Test Material (wt-%)

	Cr	Ni	Mo	Mn	Si	S	P	C	N	O	Fe
L-PBF 316L Hot Ductility Specimens	18.62	11.92	2.33	0.74	0.82	0.006	0.016	0.020	0.0833	0.0253	Bal.
L-PBF 316L GTAW Plates	17.75	12.29	2.54	0.84	0.84	0.009	0.016	0.02	0.0789	0.0258	Bal.
GMA-DED 316L	19.16	11.89	2.37	1.66	0.36	0.016	0.019	0.01	0.0282	0.0401	Bal.
GMA-DED 316LSi	18.38	11.62	2.34	1.62	0.78	0.013	0.022	0.02	0.0700	0.0272	Bal.
GMA-DED 316H	19.08	11.56	2.28	1.67	0.36	0.005	0.021	0.04	0.0786	0.0378	Bal.
Wrought 316L	16.87	10.34	2.17	1.25	0.30	0.002	0.029	0.027	0.0537	–	Bal.
Wrought 316H	17.10	10.33	2.17	1.51	0.42	0.004	0.036	0.04	0.0401	–	Bal.

Hot Ductility Testing

Hot ductility testing provides a method for understanding the cracking sensitivity of alloys during welding through a simulated weld thermal cycle and high strain rate deformation to fracture. The test is performed over a range of temperatures to determine the strength and ductility behavior of simulated weld HAZ microstructures (Ref. 4). On-cooling hot ductility tests were performed in this work using a Gleeble® 3500-GTC thermo-mechanical simulator.

R-type thermocouples were tack-welded onto the test specimens. The specimens were heated at 200°C/s up to a peak temperature, held for 2 s, cooled at 40°C/s to the chosen on-cooling test temperature, held for 2 s, and then pulled to fracture at a crosshead speed of 20 mm/s. The peak temperature for hot ductility is relatively ambiguous in the literature. Oftentimes, the nil strength temperature (NST) or nil ductility temperature (NDT) is used, or sometimes a temperature between or just below the NST and NDT is chosen. In this work, the peak temperature was chosen as NDT –20°C to avoid liquidation cracking issues. The NDT was determined for each condition through a few on-heating tests, i.e., the first temperature at which 0% RA was measured. The NDT and peak temperature for each condition are shown in Table 3.

On-cooling tests were performed between 1000°C and 1300°C in 25°C to 50°C temperature increments. After testing, the % RA of each specimen was measured six times using calipers (three measurements per failed section), and the average % RA was plotted as a function of test temperature. Duplicate testing at temperatures of interest was performed when sample quantities allowed. The force and stroke data output from the Gleeble during the hot ductility tests were converted to stress and strain. The area under the stress versus strain plot was calculated to determine absorbed energy as a function of testing temperatures.

Table 3 — Peak Temperature and NDT for Hot Ductility Testing

	Peak Testing Temperature (°C) (NDT – 20°C)	NDT (°C)
L-PBF 316L	1320°C	1340°C
GMA-DED 316 (L/H/LSi)	1330°C	1350°C
Wrought 316 (L/H)	1325°C	1345°C

Microstructure Characterization

Failed hot ductility specimens were cross-sectioned and prepared for electron backscatter diffraction (EBSD) analysis. EBSD analysis was performed using a Helios NanoLab 600i scanning electron microscope (SEM) equipped with an EDAX Hikari Super detector operating at 20 kV voltage. A subset of specimens were electrolytically etched using 10% oxalic acid (4.5 V, 1 min.) for light optical microscopy (LOM) with an Olympus DSX500 digital optical microscope. The fracture surfaces of the failed specimens were inspected using a FEI Nova NanoSEM operating at 20 kV voltage. Thin foils for scanning transmission electron microscopy (STEM) were prepared using twin-jet electropolishing in a 5% perchloric acid and 95% methanol solution at –40°C and 30 – 40 V. TEM observations were conducted in STEM mode using a FEI Talos F200X with a 200 kV accelerated voltage. The equipped EDAX EDS detector was used to confirm the presence of oxides in the microstructures.

EBSD data was processed using EDAX OIM software, where all inverse pole figure (IPF) maps were colored with the reference direction aligned with the tensile axis. MTEX, a Matlab toolbox for crystallographic analysis, was used to determine percent recrystallized from the IPF maps with the grain orientation spread parameter (Refs. 21, 22). IPF maps were acquired as close as possible (50 – 100 μm) to the fracture surface of the failed hot ductility specimens while avoiding inclusion of mounting material. For each sample condition, three IPF maps were collected along the edge of the fracture surface and used to determine the average percent recrystallized.

Constrained Gas Tungsten Arc Welding Experiments

A subset of specimens underwent an additional set of constrained GTAW experiments to relate cracking susceptibility determined from hot ductility tests to DDC susceptibility in welded test specimens. Solution annealed GMA-DED 316L and L-PBF 316L builds were milled down to a machined surface finish. The L-PBF 316L material for this portion of the study came from a secondary build produced on the same EOS M290, using the same process parameters as the hot ductility specimens, and has a very similar build composition (Table 2). The machined plates, along with a wrought 316L plate, were sectioned into 2 in. L × 1.5 in. W × 0.625 in. T (50.8 mm × 38.1 mm × 15.9 mm) samples. Two samples from each condition were fillet welded around all four sides to a 12 in. L × 3 in. W × 1.5 in. T (304.8 mm × 76.2 mm × 38.1 mm) plain carbon steel strong back using GTAW. Autogenous GTAW was performed along the 2 in. (50.8 mm) sample dimension using a gantry system and a Miller Dynasty 350 welder. A travel speed of 5 ipm (2.12 mm/s) and 250 A was used. For each condition, a single-pass weld and a three-pass weld were produced. The three-pass weld involved melting the same weld track three times to simulate aggressive reheat conditions that could be experienced in a multi-pass weld HAZ. The samples were removed from the strong back and cross-sectioned for characterization. The HAZ of the etched (electrolytic 10% oxalic acid) weld cross-sections were inspected using a TESCAN S8000G SEM in secondary electron (SE) imaging mode operating at 20 kV voltage.

Results

Starting Microstructure

Representative IPF and phase maps of the starting microstructures prior to hot ductility testing are shown in Fig. 1. The solution annealed GMA-DED 316L condition (Fig. 1A) exhibits large columnar grains with remnant δ-ferrite from solidification, shown by the inset phase map, indicating incomplete dissolution after a 1 h solution anneal at 1040°C. To evaluate the role of δ-ferrite on hot ductility behavior, a subset of GMA-DED 316L and 316LSi specimens underwent an additional heat treatment of 1150°C for 5 h to fully dissolve δ-ferrite from the microstructure. As shown in Fig. 1B, the additional heat treatment successfully dissolved δ-ferrite without altering the columnar grain morphology.

The wrought 316L condition exhibits a fine-grained, equiaxed microstructure with an average grain diameter of 49 ± 30 μm (Fig. 1C). The grain morphology of the horizontal and vertical L-PBF 316L specimens is shown in Figs. 1D and E, respectively, with corresponding IPFs shown in Figs. 1G and H. No δ-ferrite is observed in the L-PBF conditions (Fig. 1D), consistent with the primary austenite solidification mode typically reported for L-PBF 316L (Ref. 23). A <001> texture is observed for the horizontal L-PBF specimen, whereas the vertical specimen exhibits a <011> texture. The 1200°C for 2 h heat treatment resulted in full recrystallization of the L-PBF 316L specimen, shown in Fig. 1F, which was confirmed separately with kernel average misorientation (KAM) maps.

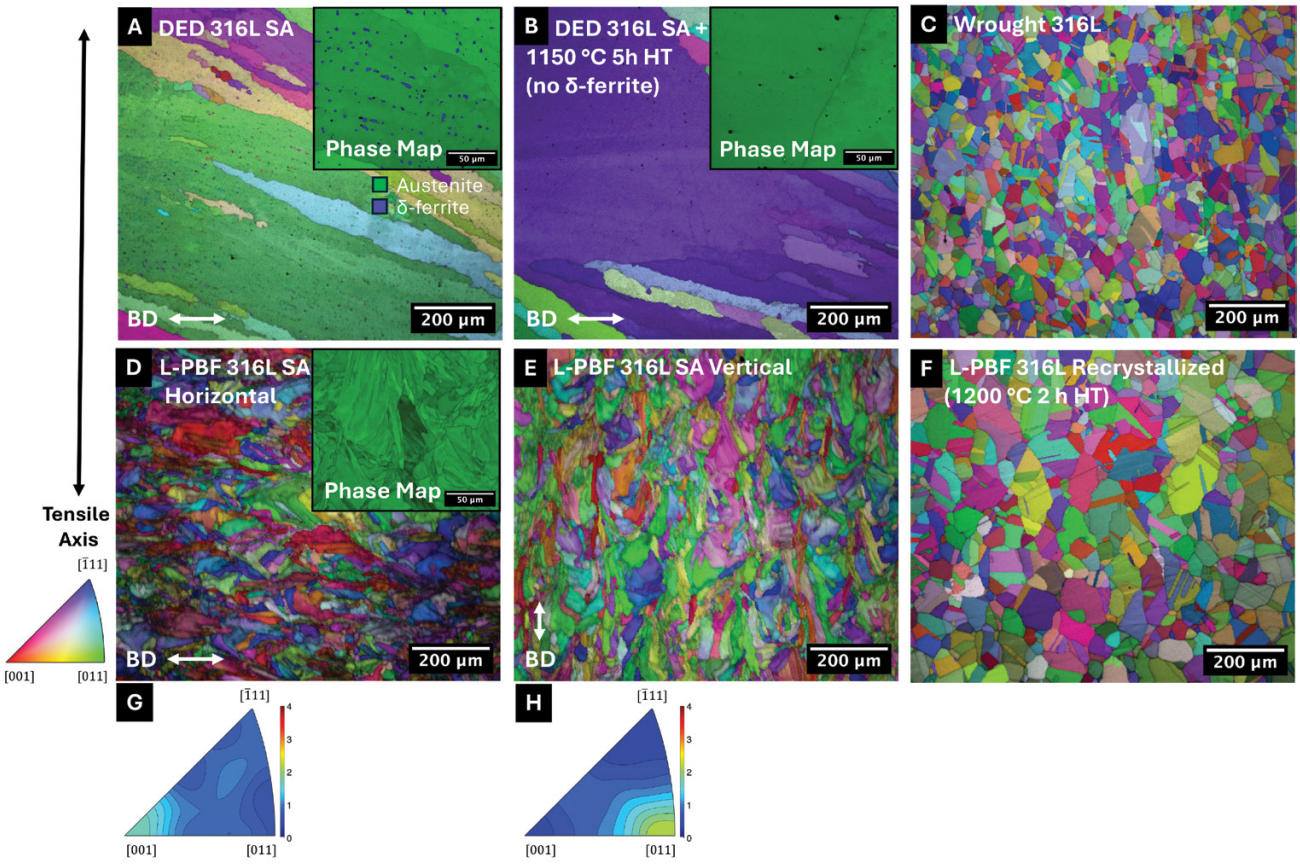


Fig. 1 — IPF and phase maps of the starting microstructures prior to hot ductility testing for: A — GMA-DED 316L; B — GMA-DED 316L heat treated at 1150°C for 5 h; C — wrought 316L; D — horizontal L-PBF 316L; E — vertical L-PBF 316L; F — recrystallized L-PBF 316L (1200°C for 2 h). Corresponding IPF for: G — horizontal; H — vertical L-PBF 316L. All IPF maps and IPFs are colorized with respect to the tensile axis. Note: the high magnification phase maps for A, B, and D. "SA" refers to solution annealed, and "BD" refers to build direction.

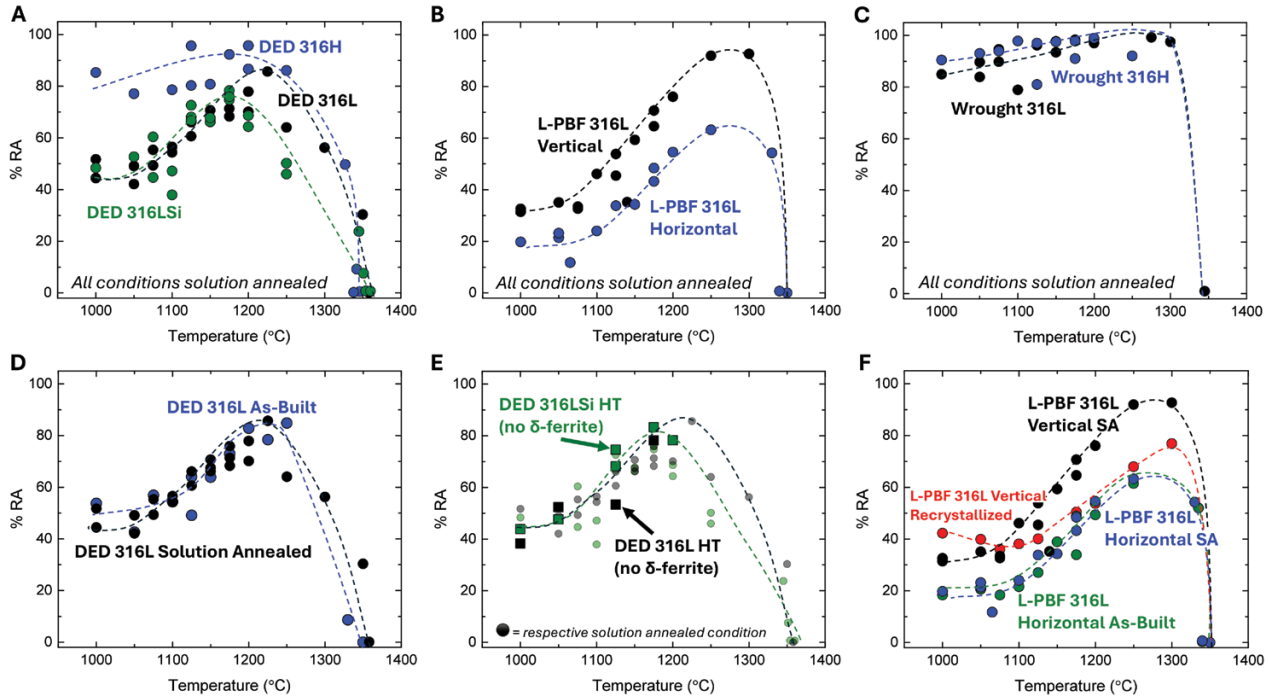


Fig. 2 — Hot ductility plots for solution annealed: A — GMA-DED; B — L-PBF; C — wrought stainless steel; and for various heat treatments of: D and E — GMA-DED; F — L-PBF stainless steel. In E — "HT" refers to 1150°C 5 h heat treatment; in F — "SA" refers to solution annealed.

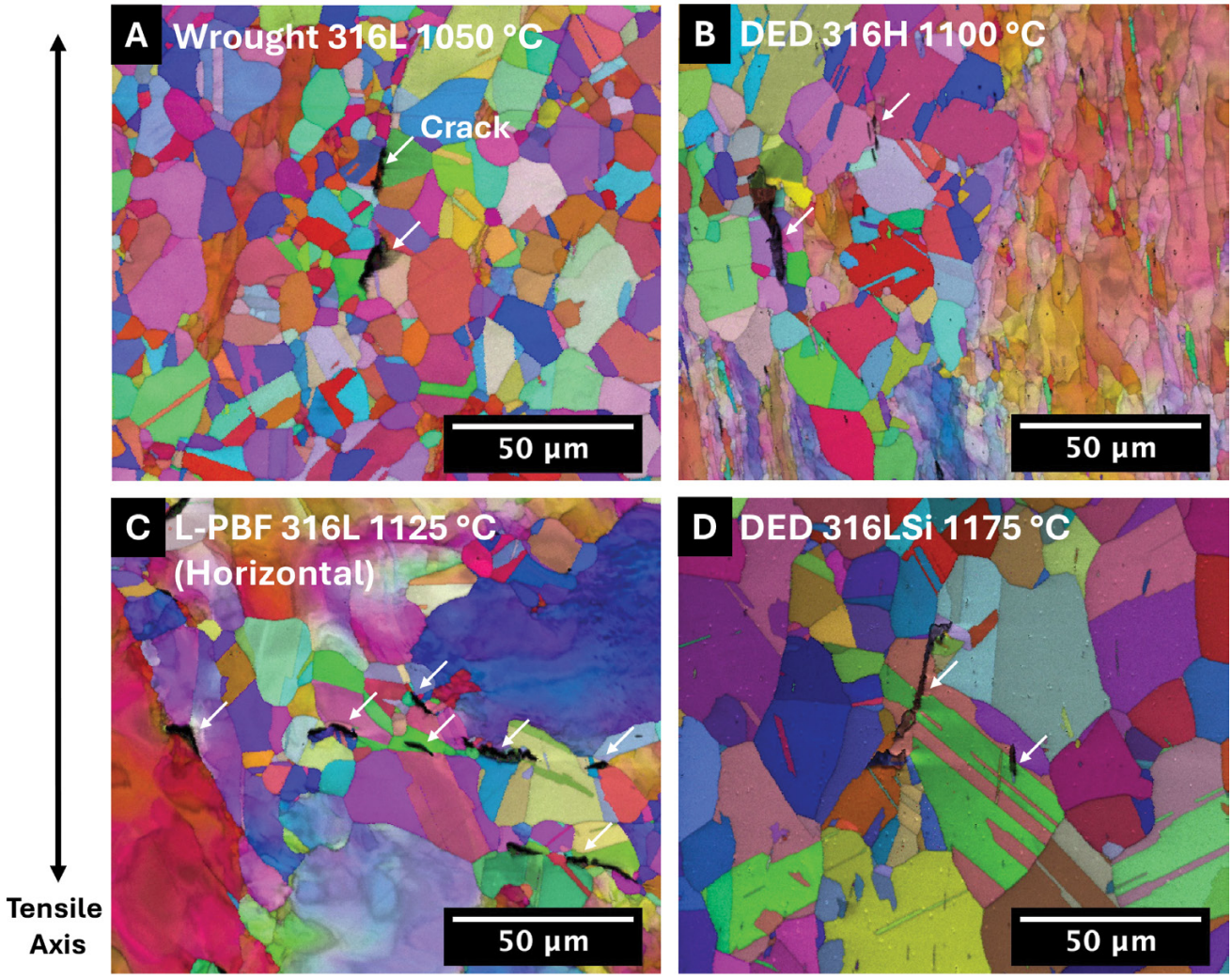


Fig. 3 — IPF maps showing small, isolated cracks (white arrows) inside recrystallized grains of hot ductility specimens: A — Wrought 316L at 1050°C; B — GMA-DED 316H at 1100°C; C — L-PBF 316L (horizontal) at 1125°C; D — GMA-DED 316LSi at 1175°C.

Hot Ductility Response

Hot ductility curves, expressed as reduction of area versus temperature, are presented in Fig. 2. Figures 2A–C show the hot ductility behavior of GMA-DED (Fig. 2A), L-PBF (Fig. 2B), and wrought (Fig. 2C) specimens, all in the solution annealed condition. Figures 2D–F show the hot ductility behavior of GMA-DED and L-PBF specimens subjected to various post-build heat treatments.

A distinct difference in ductility response is observed among the solution annealed conditions. The GMA-DED and wrought specimens exhibit relatively high ductility, whereas the L-PBF specimens exhibit reduced ductility, particularly in the horizontal orientation. The wrought material is fine-grained with low impurity levels and, as such, is expected to exhibit high ductility (Ref. 9). The ductility response of the wrought specimens confirms that the hot ductility testing method used in this study produces representative results.

Figure 2D compares the ductility response of as-built and solution annealed GMA-DED 316L, showing negligible differences between the two conditions. The additional heat treatment to dissolve δ-ferrite (1150°C for 5 h) from the GMA-DED conditions also appears to have a negligible impact on the ductility response of GMA-DED 316L and 316LSi, as shown in Fig. 2E. For the GMA-DED conditions, ductility behavior remained largely unchanged regardless of post-build heat treatment.

The ductility behavior of as-built, solution annealed, and recrystallized (1200°C for 2 h) L-PBF 316L is shown in Fig. 2F. Similarly to the GMA-DED conditions, post-build heat treatment had minimal impact on the ductility response of L-PBF 316L. The vertical and horizontal L-PBF specimens (Figs. 2B and F) exhibited anisotropic hot ductility behavior, with the vertical specimens exhibiting greater ductility than the horizontal specimens. Similar anisotropic ductility has also been observed for L-PBF 316L in Charpy impact and tensile testing, and is attributed to differences in crystallographic texture (Refs. 24, 25).

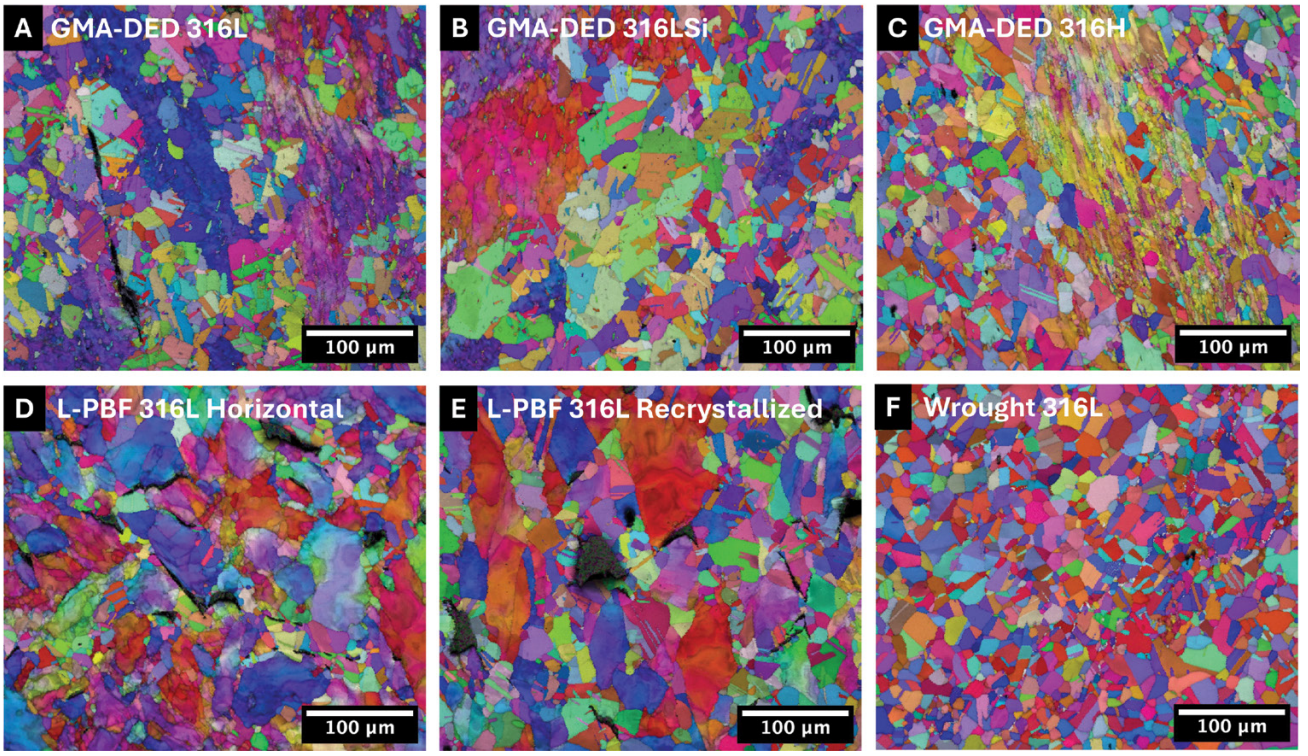


Fig. 4 — IPF maps showing various amounts of dynamic recrystallization for 1125°C hot ductility specimens: A — GMA-DED 316L; B — GMA-DED 316LSi; C — GMA-DED 316H; D — L-PBF 316L (horizontal); E — recrystallized L-PBF 316L; F — wrought 316L. Each specimen was solution annealed unless otherwise specified.

Microstructure Characterization

Dynamic recrystallization is considered an important mechanism for restoring ductility at elevated temperatures. The formation of new recrystallized grains is thought to reduce strain accumulation at grain boundaries and to inhibit or arrest crack propagation (Refs. 5, 6, 14, 26, 27). Consistent with this behavior, Fig. 3 shows small, recrystallized grains near crack tips and isolated cracks within recrystallized grains near the fracture surface of failed hot ductility specimens. Larger IPF maps were used to determine differences in recrystallization behavior as a function of test temperature and are shown in Fig. 4. Figures 4A–F show the recrystallization behavior of the GMA-DED, L-PBF, and wrought conditions at 1125°C. IPF maps at other temperatures (1000°C, 1050°C, and 1200°C) are shown in the Appendix. The percent recrystallization was determined for each condition at three different locations and averaged. The results are shown in Fig. 5.

Based on Fig. 5, trends in recrystallization behavior do not fully account for the observed hot ductility response. Wrought 316L and GMA-DED 316H specimens exhibit substantial recrystallization, consistent with their high ductility. In contrast, the other GMA-DED and L-PBF conditions exhibit similar amounts of recrystallization, despite the L-PBF conditions exhibiting a clear decrease in ductility. It would be expected that L-PBF conditions would have a strong driving force for recrystallization due to increased strain energy in the microstructure from the printing process. During static annealing, L-PBF 316L is shown to recrystallize at faster rates

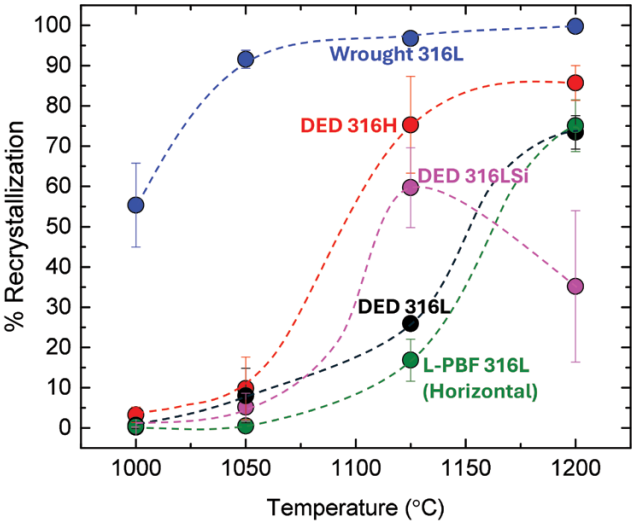


Fig. 5 — Percent recrystallization observed in hot ductility specimens as a function of testing temperature.

than GMA-DED 316L (Ref. 28). Interestingly, L-PBF 316L does not appear to have accelerated dynamic recrystallization kinetics during hot ductility testing.

Given that the extent of recrystallization does not fully correlate with the observed ductility response, an investigation into sub-surface cracking characteristics and fracture mechanisms

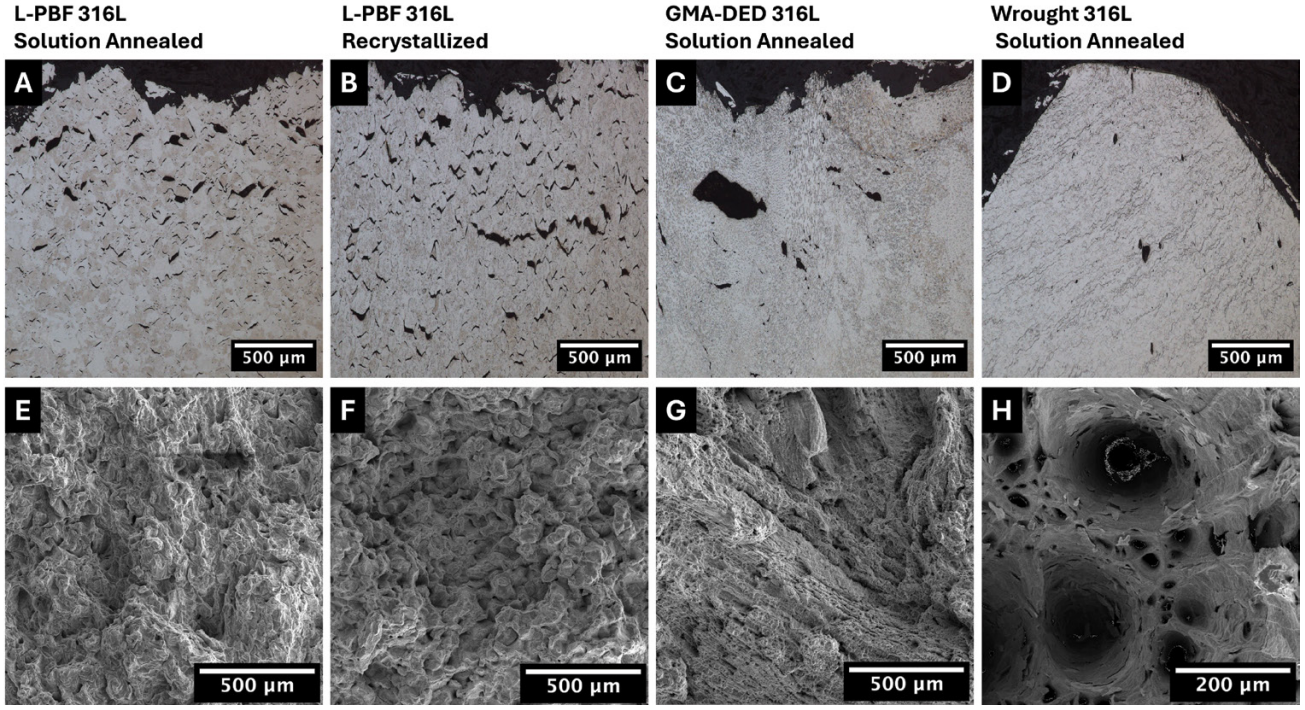


Fig. 6 — A–D — Etched LOM micrographs; E–H — SEM fracture surfaces of 1125°C hot ductility specimens. A and E — Solution annealed L-PBF 316L; B and F — recrystallized L-PBF 316L; C and G — solution annealed GMA-DED 316L; D and H — solution annealed wrought 316L.

was performed and is shown in Fig. 6. The solution annealed and recrystallized L-PBF 316L specimens (Figs. 6A and B) have an increased amount of microcracking, likely at high-angle grain boundaries, compared to the higher ductility GMA-DED 316L (Fig. 6C) and wrought 316L (Fig. 6D) specimens. The L-PBF 316L specimens (Figs. 6E and F) also display intergranular fracture behavior consistent with a higher cracking susceptibility compared to the GMA-DED 316L (Fig. 6G) and wrought 316L (Fig. 6H) specimens that exhibit ductile fracture surfaces with microvoids.

There is a clear distinction in ductility behavior, cracking characteristics, and fracture morphology between the L-PBF specimens and the other conditions, consistent with an increased susceptibility to DDC. Stress-strain curves from the hot ductility tests (Figs. 7A–D) were used to calculate absorbed energy (Fig. 7E). The solution annealed and as-built L-PBF specimens exhibit high peak stresses but limited elongation, resulting in lower overall absorbed energy compared to the wrought and GMA-DED specimens. The absorbed energy trends are consistent with the observed ductility behavior, suggesting that the difference in ductility across AM and wrought conditions is closely related to variations in absorbed energy, which is related to material toughness. Interestingly, the recrystallized L-PBF 316L specimens exhibit absorbed energy behavior comparable to the GMA-DED specimens, despite their lower ductility response and predominance of intergranular fracture. This suggests that early plastic deformation behavior is similar between the recrystallized L-PBF 316L and GMA-DED conditions, and differences likely exist in post-uniform deformation characteristics.

It has been reported that L-PBF 316L has reduced toughness in Charpy impact testing relative to wrought material. Sonis et al. reported room temperature impact energy of 170 – 250 J/cm^2 for L-PBF 316L, compared with 350 – 400 J/cm^2 for wrought 316L (Ref. 24). The reduced toughness of L-PBF 316L was attributed by the authors to oxide particles that form during solidification and are thought to act as void nucleation sites due to decohesion at the oxide/matrix interface during deformation (Refs. 24, 29–31). These nanoscale oxides are well documented in L-PBF 316L and form during the printing process due to oxygen contamination.

The oxide particles in the L-PBF 316L specimens tested in this work were investigated using STEM bright field and are shown in Fig. 8. The black particles are Si- and Mn-rich oxides, while the white features are holes where the oxide particles were removed during TEM specimen preparation. This interpretation was confirmed separately through EDS analysis. The initial size and distribution of the oxides are shown for the solution annealed condition in Figs. 8A and D. After hot ductility testing at 1050°C, no appreciable change in oxide size or distribution is observed (Figs. 8B and E). The recrystallized and tested L-PBF specimen displays appreciable coarsening of the oxides (Figs. 8C and F), where coarsening occurred during the recrystallization heat treatment due to Ostwald ripening (Ref. 30).

Recrystallized L-PBF 316L is often reported to have reduced impact toughness, which is associated with greater decohesion and void formation at the particle/matrix interface due to increased size of oxide particles and their localization to grain boundaries (Refs. 24, 29–31). In this case, larger oxides are observed for the recrystallized L-PBF 316L condition; however, the absorbed energy is higher compared to the other L-PBF conditions (Fig. 7E). This suggests that the oxides do not appear to be contributing to the differences in absorbed energy. Additionally, oxides in the solution annealed conditions are distributed throughout the microstructure, not just

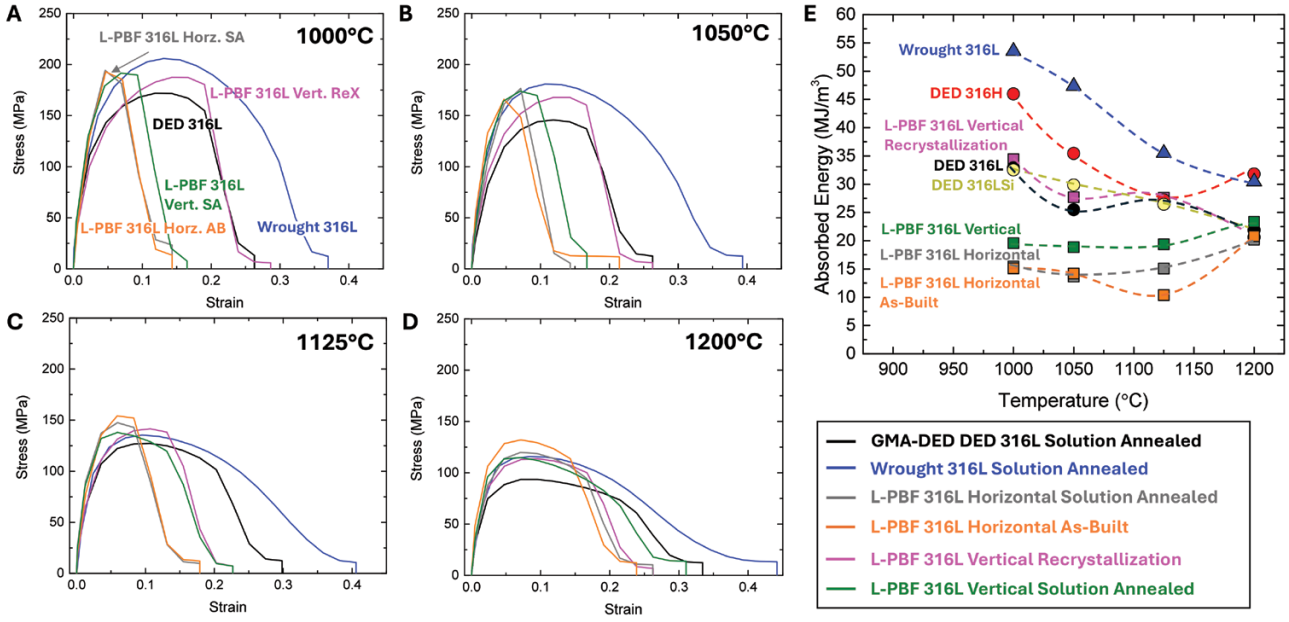


Fig. 7 — Stress versus strain curves from: A — 1000°C; B — 1050°C; C — 1125°C; D — 1200°C hot ductility tests; E — calculated absorbed energy as a function of testing temperature.

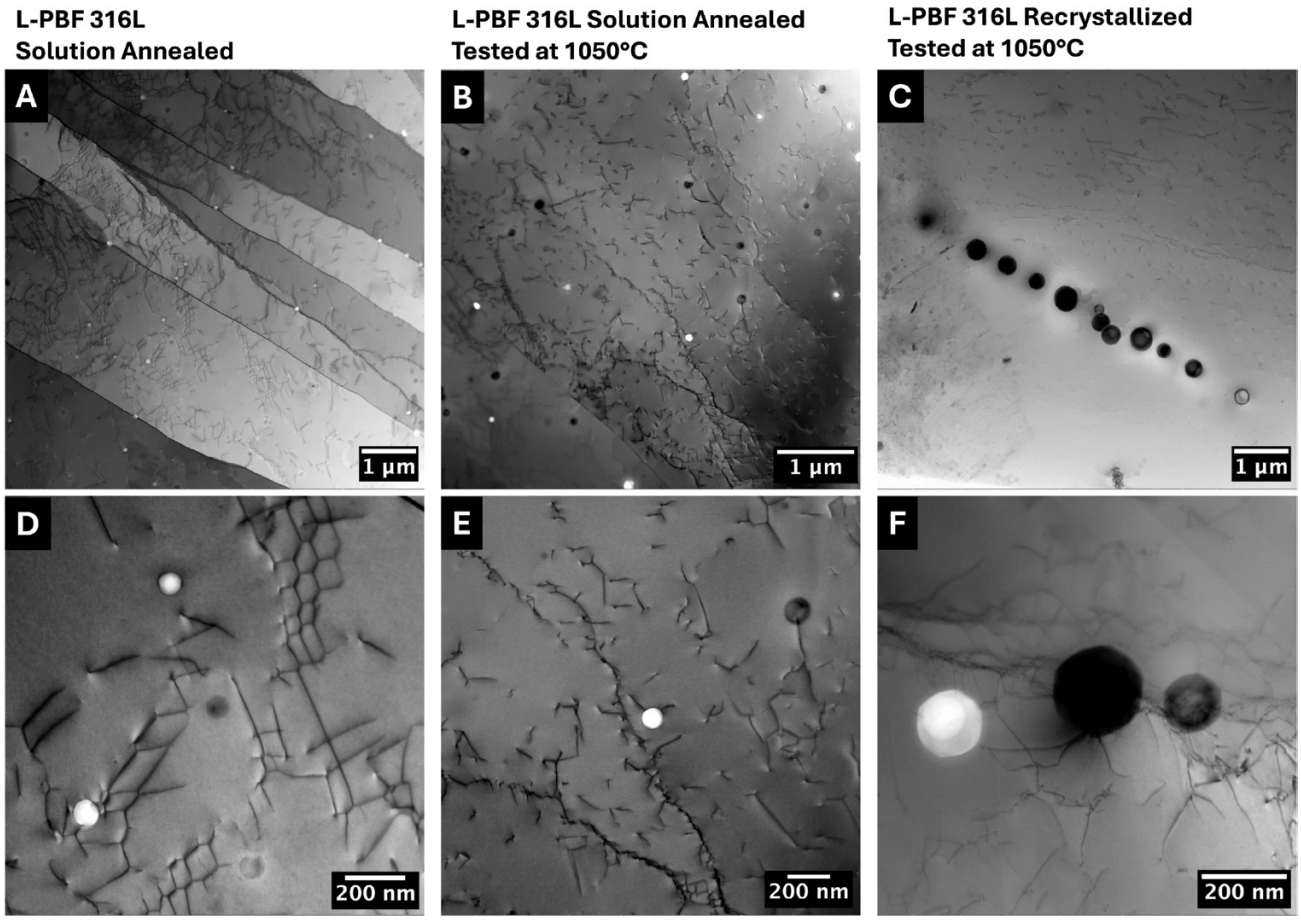


Fig. 8 — STEM bright field images showing size and distribution of oxides present in: A and D — Solution annealed L-PBF 316L; B and E — solution annealed L-PBF hot ductility specimens tested at 1050°C; C and F — recrystallized L-PBF 316L hot ductility specimens tested at 1050°C.

at grain boundaries, indicating that the oxides are unlikely to induce the grain boundary fracture exclusively observed in the L-PBF hot ductility specimens. For the recrystallized specimens, some localization of oxide particles along grain or cell boundaries is observed, which does not appear to affect hot ductility behavior.

Constrained GTAW Welds

While hot ductility testing is a useful metric for ranking cracking susceptibility, it does not directly reveal the extent of cracking in a welded component. To correlate hot ductility behavior with DDC susceptibility in a weld, constrained autogenous GTAW was performed on solution-annealed L-PBF, GMA-DED, and wrought 316L plates. Micrographs of the HAZ of the welds are shown in Fig. 9. Overview images of the welds are shown in Fig. A4 in the Appendix. No cracking was observed in the HAZ of either the single-pass or three-pass welds of wrought (Figs. 9A and B) and GMA-DED 316L (Figs. 9C and D). In the single-pass L-PBF 316L weld (Figs. 9E and F), small voids are visible within the HAZ, primarily aligned along grain boundaries and at the edges of melt pools from the L-PBF process. In the three-pass L-PBF 316L weld (Figs. 9G and H), the voids appeared to have coalesced into microcracks, indicating a susceptibility to HAZ cracking. The HAZ cracks are observed several microns away from the fusion zone, with a majority of cracks located well within the HAZ. The spatial distribution of cracks within the HAZ indicates increased cracking susceptibility at temperatures below the solidus, which appears to correlate well with the hot-ductility data, which shows a dip in ductility between 1000°C and 1100°C.

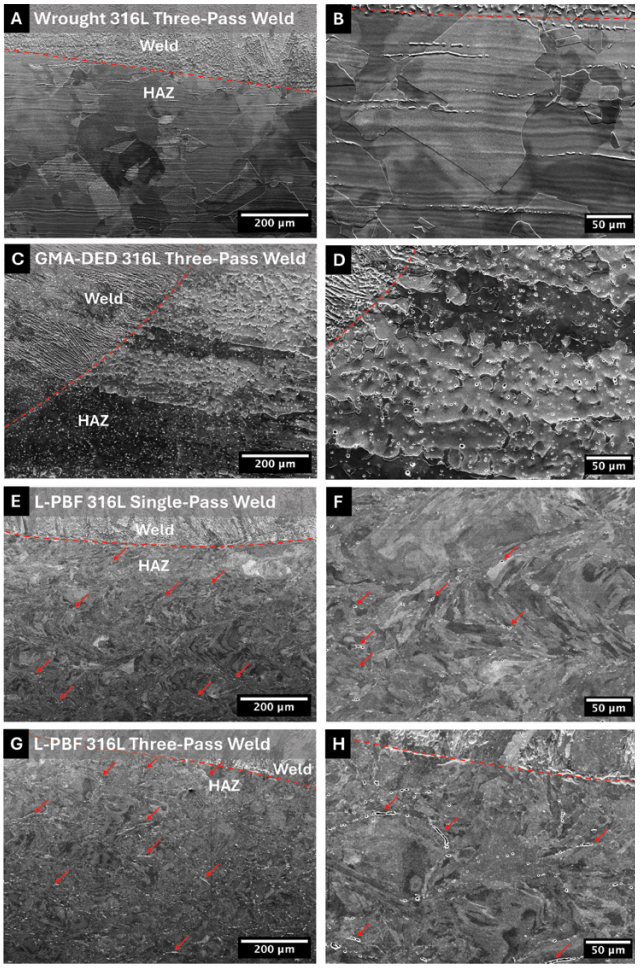


Fig. 9 — Etched GTAW HAZ of: A and B — Wrought 316L three-pass weld; C and D — GMA-DED 316L three-pass weld; E and F — L-PBF 316L single-pass weld; G and H — L-PBF 316L three-pass weld. Red arrows indicate voids and microcracks.

Discussion

Relationship Between Absorbed Energy and Nano-Scale Oxides

The results of this study demonstrate that GMA-DED 316 (L/H/LSi) specimens exhibit good hot ductility regardless of post-build heat treatment, while L-PBF 316L specimens exhibit overall reduced hot ductility. Differences in hot ductility behavior across conditions cannot be fully explained by variations in dynamic recrystallization. Rather, the variations in ductility response tend to correlate with differences in absorbed energy, which is related to material toughness. The L-PBF conditions consistently exhibit lower absorbed energy (Fig. 7E) compared to the GMA-DED and wrought conditions. An exception is the recrystallized L-PBF specimens, which exhibit higher absorbed energy but a ductility response similar to that of the other L-PBF conditions. The discrepancy between absorbed energy and % RA for the recrystallized L-PBF specimens indicates that the recrystallization heat treatment predominantly affected deformation behavior associated with yielding and early plastic flow, while having minimal influence on post-uniform plasticity, which % RA only considers.

Reduced toughness of L-PBF 316L has been reported in the literature and has been attributed to the presence of nanoscale oxide particles within the microstructure that serve as void initiation sites during deformation (Ref. 24, 29–31). In this study, the oxides were characterized and shown to maintain their size and distribution in the microstructure during hot ductility testing (Figs. 8A and B). The recrystallization heat treatment led to an increase in oxide size and some particle localization at grain and cell boundaries (Figs. 8C and F). However, the coarsening of the oxides did not correspond to a further decrease in ductility or toughness (Figs. 2F and 7E). If the oxides were primarily responsible for the reduced ductility of the L-PBF specimens, then an increase in oxide size and localization of particles at boundaries would be expected to correspond to reduced toughness as observed in literature for Charpy impact testing (Ref. 24, 30). Seeing as there was no appreciable change in ductility response for the recrystallized L-PBF specimens, the oxide particles do not appear to be negatively impacting hot ductility response.

The cracking observed at grain boundaries and the intergranular fracture behavior of the L-PBF specimens (Fig. 6) are consistent with grain boundary embrittlement. Intergranular fracture is commonly associated with the presence of grain boundary precipitates or segregation of impurity elements to grain boundaries (Ref. 32). In this study, the oxides do not appear to be preferentially located at grain boundaries,

further suggesting that they are not the likely cause of the reduced toughness and ductility of the L-PBF conditions. For the recrystallized specimens where some localization of oxides to boundaries is observed, there is no corresponding decrease in ductility, also indicating that oxides do not appear to be dictating ductility behavior. No other precipitates, such as $M_{23}C_6$-type carbides, are expected or observed within the microstructure either. Precipitation has been shown to play a critical role in the DDC behavior of Ni-based alloys, where MC and $M_{23}C_6$ precipitates form and affect grain boundary tortuosity and strain misfit, which, in turn, influence cracking behavior (Refs. 10, 15). Seeing as carbides are not present in the microstructures of this work and oxides do not appear to be affecting DDC behavior as reported for other second-phase particles, another mechanism appears to be causing grain boundary embrittlement in the L-PBF conditions.

As such, the reduced ductility of the L-PBF conditions observed in this work is attributed to segregation of impurity elements such as sulfur and phosphorus to the grain boundaries, which will be discussed further in the next section. In contrast, the GMA-DED and wrought specimens exhibit fracture surfaces with microvoids, indicative of considerable plastic deformation prior to fracture, consistent with their superior hot ductility.

Wedge cracking is another mechanism by which intergranular fracture can occur due to grain boundary sliding on precipitate-free boundaries. During sliding, wedge voids can form at triple points and lead to intergranular cracking without the presence of precipitates or grain boundary embrittlement (Ref. 10). However, while wedge cracking may contribute to damage evolution, it does not explain the observed differences in ductility behavior across test conditions or the intergranular fracture behavior of just the L-PBF specimens. As such, impurity segregation provides a reasonable explanation for the observed differences in behavior as it can reduce grain boundary cohesion and promote intergranular separation under similar deformation conditions.

The L-PBF specimens also exhibit anisotropic ductility, with the vertical orientation showing better hot ductility than the horizontal orientation. Similar anisotropic ductility behavior has been reported by others (Refs. 24, 25, 30) and is attributed to differences in crystallographic texture based on build orientation. Vertical specimens aligned with the build direction exhibit a <011> fiber texture with respect to the tensile axis, which corresponds to greater ductility than horizontal specimens with a <001> fiber texture with respect to the tensile axis shown by the IPFs in Fig. 1. This texture-ductility relationship observed is consistent with literature and is largely associated with the activation of different deformation mechanisms depending on crystallographic texture (Refs. 24, 25, 30).

Impact of Impurity Elements and Primary Solidifying Phase on Hot Ductility Response

Impurity elements such as sulfur and phosphorus, which are melting point-suppressing elements, are known to segregate to interdendritic regions and eventually grain boundaries during solidification because they are the last regions to solidify. This type of impurity segregation has been shown to lead to increased DDC susceptibility (Refs. 33, 34). Based on the build compositions reported in Table 2, the L-PBF builds do not exhibit elevated sulfur content, especially compared to the GMA-DED builds. The key difference between the GMA-DED and L-PBF builds is the primary solidification mode (PSM), which is likely to affect the local impurity content at grain boundaries.

The GMA-DED builds solidify as a primary ferrite secondary austenite (FA) mode, where δ-ferrite solidifies first, and partially transforms to austenite upon cooling. The resulting microstructure consists of skeletal δ-ferrite at the dendrite cores in an austenite matrix. δ-ferrite has a high solubility for impurity elements like sulfur, which is known to be beneficial in reducing solidification cracking susceptibility of austenitic stainless steels (Ref. 35). In this study, the GMA-DED specimens exhibited similar hot ductility behavior across all post-build heat treatment (as-built, partial solution anneal, and complete solution anneal with no δ-ferrite), indicating that the presence of δ-ferrite in the microstructure during testing is less important than the fact that δ-ferrite formed first during solidification. During FA solidification, sulfur and other impurities will preferentially partition to δ-ferrite, which is located at the dendrite core, away from interdendritic regions that ultimately form grain boundaries. Even with complete dissolution of δ-ferrite through heat treatment, the hot ductility response remains high. Although sulfur diffusion to grain boundaries during the 1150°C dissolution heat treatment is kinetically feasible, there is no corresponding change in ductility. This indicates that there may not be sufficient driving force or concentration gradient for impurity segregation to grain boundaries due to the dissolution of δ-ferrite at dendrite cores, far away from grain boundaries. Rather, the impurity elements may redistribute uniformly within the austenite matrix, thereby minimizing their deleterious effects on ductility and toughness.

For the L-PBF builds, the increased solidification velocity of the printing process stabilizes the austenite phase relative to δ-ferrite, and as a result, L-PBF 316L solidifies as primary austenite (Ref. 36). During primary austenite solidification, impurity elements will preferentially segregate to interdendritic regions and grain boundaries, leading to local sulfur enrichment, which likely increases susceptibility to cracking. Random walk diffusion distance estimates for sulfur were calculated using reported diffusivity data (Ref. 37). These calculations indicate that the time at elevated temperature during the hot ductility testing and post-build heat treatments is sufficient for sulfur to diffuse over distances comparable to the primary dendrite arm spacing and grain size of the L-PBF 316L microstructure. This suggests that sulfur can segregate to grain boundary regions during testing and heat treatment, if it was not already present there from solidification. During the 1200°C recrystallization heat treatment, sulfur likely diffuses to newly formed recrystallized grain boundaries, which may explain why the recrystallized L-PBF specimens exhibited a similar hot ductility response to the other L-PBF conditions. During recrystallization, grain boundary migration can also drag solutes along, which may contribute to continued impurity segregation. Comparatively, during the δ-ferrite dissolution heat treatment for the GMA-DED specimens, there is no movement of austenite grain boundaries, so no

possible solute drag to encourage grain boundary segregation as there may be with the recrystallization heat treatment.

The detrimental impact of impurity elements on HAZ cracking was investigated in early work related to the overall hot cracking susceptibility of austenitic stainless steels (Refs. 16, 34). Li et al. investigated Type 308 welds with varying sulfur and phosphorus levels and concluded that reducing impurity content in the base metal was more effective in minimizing HAZ cracking than the presence of δ-ferrite (Ref. 17). Similarly, Kujanpää et al. used Auger electron spectroscopy to detect significant sulfur enrichment at HAZ crack surfaces of Type 310 welds relative to the bulk composition. Their results showed lower DDC susceptibility in the laboratory heats containing 0.006 to 0.008 wt-% S compared to commercial heats containing 0.007 to 0.015 wt-% S. In all their welds, the HAZ contained no δ-ferrite (Ref. 33).

The relationship between HAZ cracking and reduced hot ductility behavior is evident in this work with the GTAW welds (Fig. 9), which show clear microcracks in the HAZ of the L-PBF specimens. Although the L-PBF 316L builds do not exhibit higher bulk sulfur contents compared to the GMA-DED builds, the location of the sulfur in the microstructure, governed by the primary solidifying phase, appears to have the greatest influence on cracking susceptibility. Furthermore, the overall lower toughness of the L-PBF material, as demonstrated during the hot ductility testing, may result in a reduced threshold for sulfur-induced cracking relative to other product forms. Additionally, the L-PBF plates have slightly higher sulfur content than the L-PBF hot ductility specimens (Table 2), which may lead to worse cracking behavior.

It is also noteworthy that the GMA-DED 316H specimens exhibited the best hot ductility behavior among the GMA-DED alloys, consistent with the lowest measured sulfur content out of all the GMA-DED alloys (Table 2). This result suggests that further improvements in process cleanliness and reduction of impurity levels in the GMA-DED builds could yield additional improvements in hot ductility response and overall weldability.

Direct characterization of impurity elements such as sulfur and phosphorus at grain boundaries is extremely difficult at the concentration levels relevant to the material in this work (60–160 ppm S). Conventional site-specific analysis techniques like energy dispersive x-ray spectroscopy (EDS) lack the sensitivity to resolve such low elemental concentrations, necessitating the use of advanced high-resolution techniques such as Auger electron spectroscopy (AES), time-of-flight secondary ion mass spectrometry (TOF-SIMS), or atom probe tomography (ATP). Each of those techniques comes with a unique set of challenges, including the need for in-situ fracture under vacuum (AES), spectra overlap and quantification challenges (TOF-SIMS), and laborious sample preparation with limited sampling volume (APT). Based on some of these limitations, direct measurement of grain boundary segregation was beyond the scope of this work.

The experimental result of this work indicates that the mechanisms commonly associated with DDC and impact grain boundary sliding, including precipitate behavior and variation in dynamic recrystallization, do not account for the differences in hot ductility response across the conditions tested. Although trends in toughness broadly correlate with hot ductility behavior, the mechanism typically associated with reduced impact toughness of L-PBF 316L again does not fully account for the measured ductility response of L-PBF 316L. Based on this, and considering the distinct solidification modes of the different AM conditions, grain boundary segregation of impurity elements is proposed as the likely mechanism dictating DDC susceptibility in AM stainless steels. This finding is consistent with prior literature (Refs. 11, 16, 19, 20, 33, 38). The exact mechanism by which impurity segregation influences cracking behavior is unclear and has been attributed to a reduction in grain boundary cohesive strength, the formation of sulfide-based intermetallic phases, or the formation of liquid films along grain boundaries, similar to a liquation cracking phenomenon (Refs. 33, 39, 40). Assessment of these mechanisms requires further work involving advanced high-resolution characterization techniques to directly characterize the grain boundary chemistry in AM stainless steels.

Weldability Considerations for AM Austenitic Stainless Steels

With modernized steelmaking practices, desulfurization and other refining processes have advanced to the point that wrought austenitic stainless steels now contain extremely low levels of sulfur and other impurity elements. This is reflected in the wrought 316L tested in this study and emphasized by the shallow melt pool depth of the GTAW welds shown in Fig. A4 (Appendix). After early investigations into DDC in wrought stainless steels in the late 1970s to 1990s (Refs. 16, 17, 33, 34), limited additional research has been conducted, possibly because impurity concentrations in modern wrought stainless steels are sufficiently low that DDC is not an issue.

In contrast, the results of this study demonstrate that DDC is a concern for AM alloys, specifically L-PBF 316L. The increased susceptibility of AM alloys to DDC may also be related to characteristics of feedstock manufacturing, along with the primary solidifying phase. As mentioned, wrought alloys are exceptionally clean, effectively eliminating DDC concerns. For GMA-DED, wire manufacturers often impose tighter compositional requirements on incoming feedstock than specified in AWS A5.9 to prevent wire drawing issues (Ref. 41). This, combined with the FA solidification mode of the GMA-DED builds, likely contributes to the good weldability performance of GMA-DED stainless steel alloys.

In comparison, 316L powder is required to meet the compositional limits defined in ASTM F3184, but it is unclear if any additional impurity controls are imposed during powder production (Ref. 42). Most commercial 316L powders are produced by air or vacuum induction melting followed by argon or nitrogen gas atomization (Ref. 43). The cleanliness of the initial feedstock for induction melting, which can be steel ingots or elemental powders, is often unspecified. Consequently, powder production involves multiple processing steps, each of which introduces potential sources for additional impurity contamination not typically present in wrought or wire production. Any issues with powder cleanliness are further exacerbated with L-PBF 316L due to the fully austenitic solidification mode, which appears to lead to increased sensitivity to impurity content. As such, the combined effects of powder cleanliness and solidification mode likely contribute to the reduced weldability and increased susceptibility of L-PBF

316L to DDC. Notably, solution annealing and recrystallization heat treatments had minimal impact on improving the weldability response of L-PBF 316L, indicating that enhanced weldability is more likely to be achieved through improved control over build composition rather than optimization of post-build heat treatments.

The reduced weldability of L-PBF 316L is reflected in reduced hot ductility and the presence of HAZ microcracks in autogenous GTAW welds. The observed HAZ microcracks are small, likely due to the solution annealed condition of the L-PBF 316L plate and the minimal constraint imposed on the GTAW welds. It is expected that as-built L-PBF 316L components could exhibit greater cracking due to residual stresses. While that was not observed with the as-built L-PBF hot ductility specimens, the residual stresses of a printed component are expected to be greater than those in the specimens tested in this work and would likely increase cracking susceptibility. In practical application settings, AM components could be large, requiring higher welding heat inputs and experience increased constraint, both of which would likely result in increased cracking. Overall, the findings of this study indicate that the fusion welding of L-PBF 316L components for integration into power generation systems may present a challenge.

Conclusions

Hot ductility testing of GMA-DED, L-PBF, and wrought 316-series stainless steels was performed to evaluate the weldability of AM austenitic stainless steels. The hot ductility behavior of each condition was investigated by characterizing differences in dynamic recrystallization, absorbed energy, and fracture mechanism. Autogenous GTAW welds were performed on a subset of specimens to correlate hot ductility behavior with DDC susceptibility. The key conclusions are as follows:

- GMA-DED 316 (L/H/LSi) specimens exhibited consistently good hot ductility, regardless of post-build heat treatment or the presence of δ-ferrite in the microstructure. L-PBF 316L specimens exhibited a reduced hot ductility response across all conditions tested. The wrought 316 L/H specimens exhibited excellent hot ductility.
- Variations in dynamic recrystallization across the conditions did not fully explain the hot ductility behavior, seeing as the L-PBF and GMA-DED conditions showed similar amounts of recrystallization but exhibited different hot ductility behavior. Variations in absorbed energy matched hot ductility trends and indicated that the L-PBF 316L specimens have low toughness, contributing to reduced ductility and intergranular fracture.
- L-PBF specimens exhibit intergranular fracture consistent with grain boundary embrittlement, whereas the GMA-DED and wrought specimens exhibit ductile fracture surfaces consisting of microvoids. The presence of oxides in the L-PBF did not correlate with reduced toughness or grain boundary embrittlement, suggesting that segregation of impurity elements to grain boundaries is a possible mechanism dictating ductility behavior.
- The fully austenitic solidification mode of L-PBF 316L indicates likely preferential segregation of impurity elements to interdendritic regions and ultimately grain boundaries, which is associated with increasing DDC susceptibility. In contrast, the GMA-DED alloys solidify in FA mode, which promotes segregation of impurity elements into δ-ferrite rather than at grain boundaries, likely reducing susceptibility. Wrought alloys exhibit exceptionally low impurity levels, so DDC is unlikely. Impurity level control varies across the production processes for plate, wire, and powder feedstock, and this variation is likely to affect the cleanliness of the starting material.
- Microcracks in the HAZ of the L-PBF GTAW welds confirmed increased DDC susceptibility of L-PBF 316L. The GMA-DED and wrought 316L welds remained crack-free. There was good agreement between the cracking susceptibility determined from hot ductility tests and the GTAW weldability study.
- Overall, this work highlights that L-PBF 316L has reduced hot ductility and is more susceptible to DDC than other 316 product forms, likely due to preferential segregation of impurity elements to grain boundaries because of primary austenite solidification. DDC susceptibility is expected to be worse in the as-built condition or in high constraint welds typical in application settings. Therefore, reduced weldability may present significant challenges for the implementation of L-PBF components in structural applications.

Acknowledgements

The authors acknowledge support from the Manufacturing and Materials Joining Innovation Center (Ma^2JIC), a National Science Foundation Industry University Cooperative Research Center (IUCRC). This material is based upon work supported by the National Science Foundation under Grant Number (2052819). Any opinions, findings, and conclusions or recommendations expressed in this material are those of the author(s) and do not necessarily reflect the views of the National Science Foundation. Data analysis was supported by instrumentation that was acquired through the support of the National Science Foundation (DMR-1828454).

References

1. Albert, M., and Gandy, D. 2020. Vision of advanced manufacturing technology (AMT) use in the nuclear industry.

2. Albert, M., and Tate, S. 2020. Quick insight brief: Directed energy deposition-additive manufacturing. *EPRI*.

3. Kou, S. 2002. Welding metallurgy. John Wiley & Sons, Hoboken, N.J. DOI: 10.1002/0471434027

4. Weiss, B. G., Grotke, G. E., and Stickler, R. 1970. Physical metallurgy of hot ductility testing. *Welding Journal* 49.

5. Mintz, B., and Crowther, D. N. 2010. Hot ductility of steels and its relationship to the problem of transverse cracking in continuous casting. *International Materials Reviews* 55: 168–196. DOI: 10.1179/095066009X12572530170624

6. Collins, M. G., Ramirez, A., and Lippold, J. 2003. An investigation of ductility dip cracking in nickel-based weld metals — Part I. *Welding Journal* 82: 288s–295s.

7. Nissley, N. E., and Lippold, J. C. 2008. Ductility-dip cracking susceptibility of nickel-based weld metals — Part 1: Strain-to-fracture testing. *Welding Journal* 87: 257–264.

8. Nissley, N. E., Collins, M. G., Guaytima, G., and Lippold, J. C. 2002. Development of the strain-to-fracture test for evaluating ductility-dip cracking in austenitic stainless steels and Ni-base alloys. *Welding in the World* 46: 32–40. DOI: 10.1007/BF03263388

9. Mintz, B., Shaker, M., and Crowther, D. N. 1997. Hot ductility of an austenitic and a ferritic stainless steel. *Materials Science and Technology* 13: 243–250. DOI: 10.1179/mst.1997.13.3.243

10. Ramirez, A. J., and Lippold, J. C. 2004. High temperature behavior of Ni-base weld metal. *Materials Science and Engineering A* 380: 245–258. DOI: 10.1016/j.msea.2004.03.075

11. Nishimoto, K., Saida, K., and Okauchi, H. 2006. Microcracking in multipass weld metal of alloy 690 Part 1 — Microcracking susceptibility in reheated weld metal. *Science and Technology of Welding and Joining* 11: 455–461. DOI: 10.1179/174329306X94291

12. Nissley, N. E., and Lippold, J. C. 2009. Ductility-dip cracking susceptibility of nickel-based weld metals — Part 2: Microstructural characterization. *Welding Journal* 88.

13. Luther, S. J., Alexandrov, B. T., McCracken, S. L., and Tatman, J. K. 2022. Correlation of imposed mechanical energy with ductility-dip cracking in a highly restrained weld of Alloy 52. *Journal of Manufacturing Processes* 79: 767–788. DOI: 10.1016/j.jmapro.2022.05.027

14. McQueen, H. J., and Jonas, J. J. 1975. Recovery and recrystallization during high temperature deformation. *Treatise on Materials Science and Technology* 393–493. DOI: 10.1016/B978-0-12-341806-7.50014-3

15. Young, G. A., Capobianco, T. E., Penik, M. A., Morris, B. W., and McGee, J. J. 2008. The mechanism of ductility dip cracking in nickel-chromium alloys. *Welding Journal* 87: 31.

16. Arata, Y., Matsuda, F., and Katayama, S. 1977. Solidification crack susceptibility in weld metals of fully austenitic stainless steels (Report II): Effect of ferrite, P, S, C, Si and Mn on ductility properties of solidification brittleness. *Transactions of JWRI* 6: 105–116.

17. Li, L., and Messler, R. W. 1999. The effect of phosphorus and sulfur on susceptibility to weld hot cracking in austenitic stainless steels. *Welding Journal* 78.

18. Nishimoto, K., Saida, K., Okauchi, H., and Ohta, K. 2006. Microcracking in multipass weld metal of alloy 690 Part 2 — Microcracking mechanism in reheated weld metal. *Science and Technology of Welding and Joining* 11: 462–470. DOI: 10.1179/174329306X94309

19. Nishimoto, K., Saida, K., Okauchi, H., and Ohta, K. 2006. Microcracking in multipass weld metal of alloy 690 Part 3 — Prevention of microcracking in reheated weld metal by addition of La to filler metal. *Science and Technology of Welding and Joining* 11: 471–479. DOI: 10.1179/174329306X94318

20. Mori, H., and Nishimoto, K. 2005. Effect of sulfur contents and welding thermal cycles on reheat cracking susceptibility in multi-pass weld metal of Fe-36%Ni alloy. *Proceedings of the KWS Conference* 377–379.

21. Barrett, C. D., Imandoust, A., Oppedal, A. L., Inal, K., Tschopp, M. A., and El Kadiri, H. 2017. Effect of grain boundaries on texture formation during dynamic recrystallization of magnesium alloys. *Acta Materialia* 128: 270–283. DOI: 10.1016/j.actamat.2017.01.063

22. Hadadzadeh, A., Mokdad, F., Wells, M. A., and Chen, D. L. 2018. A new grain orientation spread approach to analyze the dynamic recrystallization behavior of a cast-homogenized Mg-Zn-Zr alloy using electron backscattered diffraction. *Materials Science and Engineering A* 709: 285–289. DOI: 10.1016/j.msea.2017.10.062

23. Dépinoy, S. 2022. Influence of solidification conditions on chemical heterogeneities and dislocations patterning in additively manufactured 316L stainless steel. *Materialia* 24: 101472. DOI: 10.1016/j.mtla.2022.101472

24. De Sonis, E., Dépinoy, S., Giroux, P. -F., Maskrot, H., Wident, P., Hercher, O., Villaret, F., and Gourgues-Lorenzon, A. -F. 2023. Microstructure–toughness relationships in 316L stainless steel produced by laser powder bed fusion. *Materials Science and Engineering A* 877: 145179. DOI: 10.1016/j.msea.2023.145179

25. Wang, X., Muñiz-Lerma, J.A., Attarian Shandiz, M., Sanchez-Mata, O., and Brochu, M. 2019. Crystallographic-orientation-dependent tensile behaviours of stainless steel 316L fabricated by laser powder bed fusion. *Materials Science and Engineering A* 766: 138395. DOI: 10.1016/j.msea.2019.138395

26. Collins, M. G., Ramirez, A., and Lippold, J. 2004. An investigation of ductility dip cracking in nickel-based weld metals — Part III. *Welding Journal* 83: 39s–49s.

27. Ramirez, A. J., and Lippold, J. C. 2005. New insight into the mechanism of ductility-dip cracking in Ni-base weld metals. *Hot Cracking Phenomena in Welds* 19–41. DOI: 10.1007/3-540-27460-X_2

28. Schreiber, M., Speer, J. G., Klemm-Toole, J., Gockel, J., Brice, C., and Findley, K. O. 2024. Influence of annealing on microstructures and mechanical properties of laser powder bed fusion and wire arc directed energy deposition additively manufactured 316L. *Materials Science and Engineering* A 917: 147390. DOI: 10.1016/j.msea.2024.147390

29. Wang, X., Sanchez-Mata, O., Atabay, S. E., Muñiz-Lerma, J. A., Attarian Shandiz, M., and Brochu, M. 2021. Crystallographic orientation dependence of Charpy impact behaviours in stainless steel 316L fabricated by laser powder bed fusion. *Additive Manufacturing* 46: 102104. DOI: 10.1016/j.addma.2021.102104

30. Deng, P., Song, M., Yang, J., Pan, Q., McAllister, S., Li, L., Prorok, B. C., and Lou, X. 2022. On the thermal coarsening and transformation of nanoscale oxide inclusions in 316L stainless steel manufactured by laser powder bed fusion and its influence on impact toughness. *Materials Science and Engineering A* 835: 142690. DOI: 10.1016/j.msea.2022.142690

31. Lou, X., Andresen, P. L., and Rebak, R. B. 2018. Oxide inclusions in laser additive manufactured stainless steel and their effects on impact toughness and stress corrosion cracking behavior. *Journal of Nuclear Materials* 499: 182–190. DOI: 10.1016/j.jnucmat.2017.11.036

32. Paupler, P., and Dieter, G. E. 1988. Mechanical metallurgy. 3rd ed. *Crystal Research and Technology* 23: 194–194. DOI: 10.1002/crat.2170230211

33. Kujanpää, V. P., David, S. A., and White, C. L. 1987. Characterization of heat-affected zone cracking in austenitic stainless steel welds. *Welding Journal* 66: 221s.

34. Shanker, V., Gill, T. P. S., Mannan, S. L., and Rodriguez, P. 1991. A review of hot cracking in austenitic stainless steel weldments. *Indira Gandhi Centre for Atomic Research*.

35. Brooks, J. A., and Thompson, A. W. 1991. Microstructural development and solidification cracking susceptibility of austenitic stainless steel welds. *International Materials Reviews* 36: 16–44. DOI: 10.1179/imr.1991.36.1.16

36. Lippold, J. C. 1994. Solidification behavior and cracking susceptibility of pulsed-laser welds in austenitic stainless steels. *Welding Journal* 73: 11.

37. Smithells, C. 2013. Metals reference book. Elsevier. DOI: 10.1016/C2013-0-06300-1

38. Li, L., and Messler, R. W. 1999. The effects of phosphorus and sulfur on susceptibility to weld hot cracking in austenitic stainless steels. *Welding Journal* 78: 387s.

39. Yamaguchi, S., Kobayashi, H., Matsumiya, T., and Hayami, S. 1979. Effect of minor elements on hot workability of nickel-base superalloys. *Metal Technology* 6: 170–175. DOI: 10.1179/030716979803276110

40. Holt, R. T., and Wallace, W. 1976. Impurities and trace elements in nickel-base superalloys. *International Metals Reviews* 21: 1–24. DOI: 10.1179/imtr.1976.21.1.1

41. AWS A5.9. 2022. Specification for bare stainless steel welding electrodes and rods. American Welding Society.

42. ASTM International. ASTM F3184. Specification for additive manufacturing stainless steel alloy (UNS S31603) with powder bed fusion. DOI: 10.1520/F3184-16R23

43. Kassym, K., and Perveen, A. 2020. Atomization processes of metal powders for 3D printing. *Materials Today: Proceedings* 26: 1727–1733. DOI: 10.1016/j.matpr.2020.02.364

Appendix

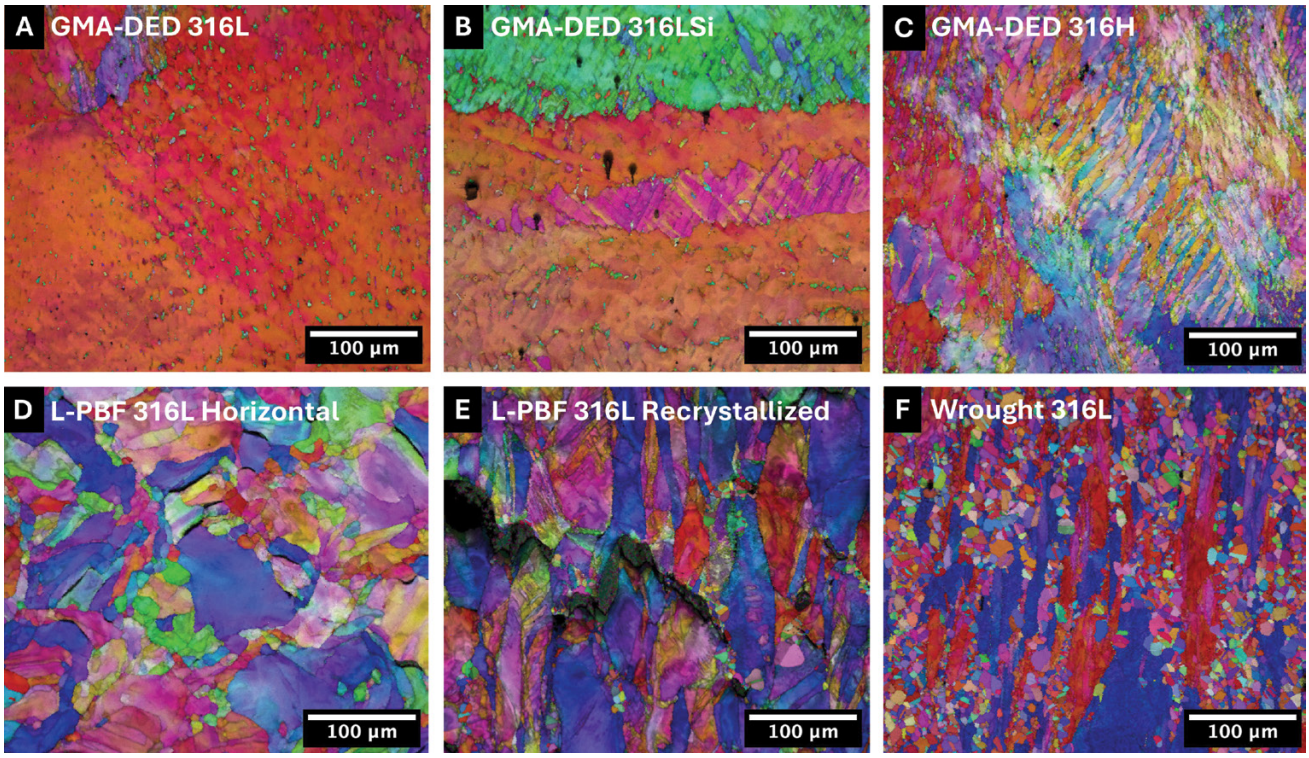


Fig. A1 — IPF maps showing various amounts of dynamic recrystallization at 1000°C: A — GMA-DED 316L; B — GMA-DED 316LSi; C — GMA-DED 316H; D — L-PBF 316L (horizontal); E — recrystallized L-PBF 316L; F — wrought 316L.

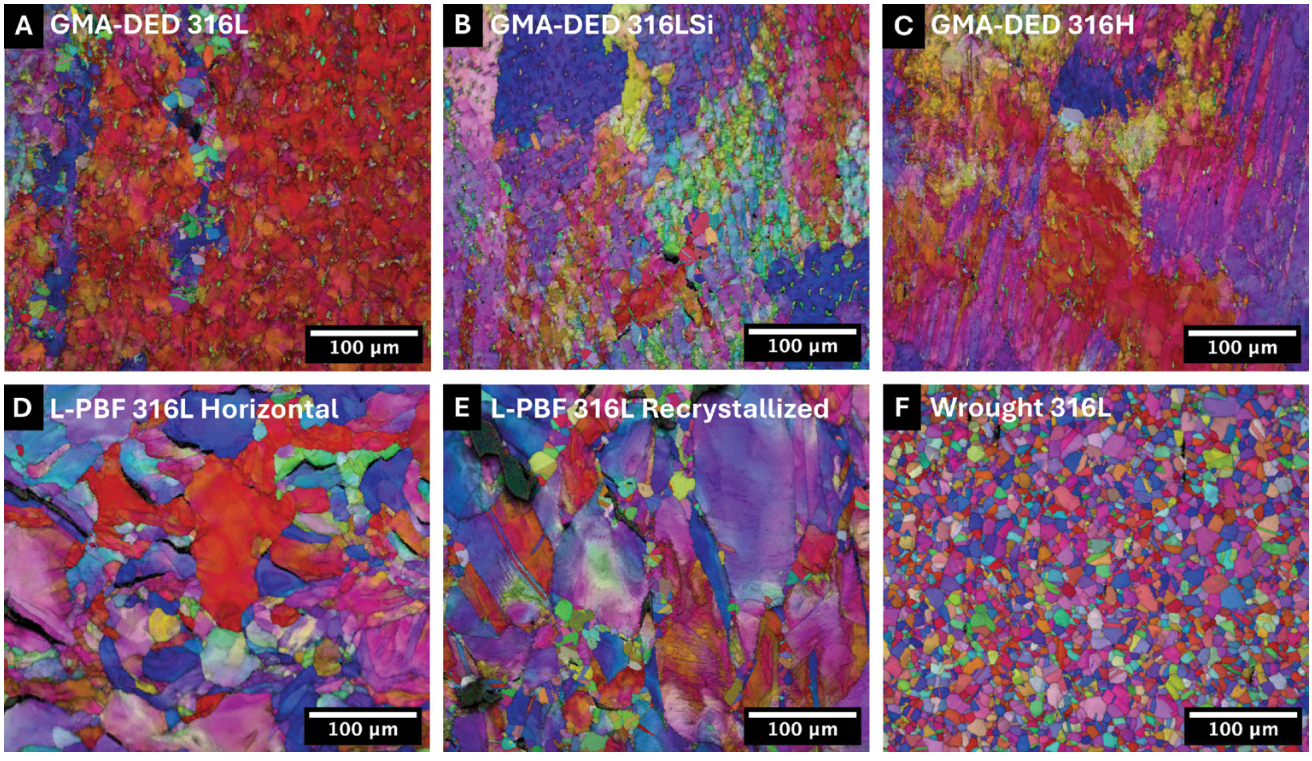


Fig. A2 — IPF maps showing various amounts of dynamic recrystallization at 1050°C for: A —GMA-DED 316L; B — GMA-DED 316LSi; C — GMA-DED 316H; D — L-PBF 316L (horizontal); E — recrystallized L-PBF 316L; F — wrought 316L.

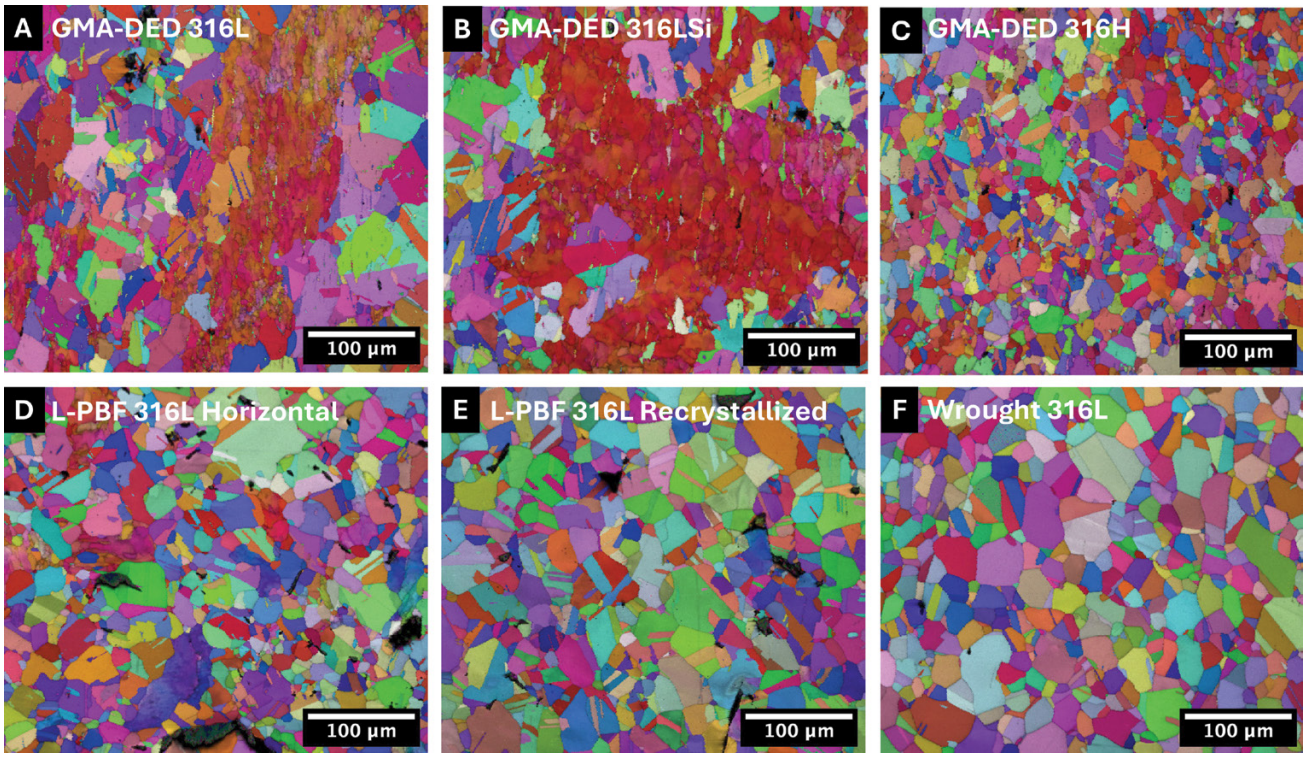


Fig. A3 — IPF maps showing various amounts of dynamic recrystallization at 1200°C for: A — GMA-DED 316L; B — GMA-DED 316LSi; C — GMA-DED 316H; D — L-PBF 316L (horizontal); E — recrystallized L-PBF 316L; F — wrought 316L.

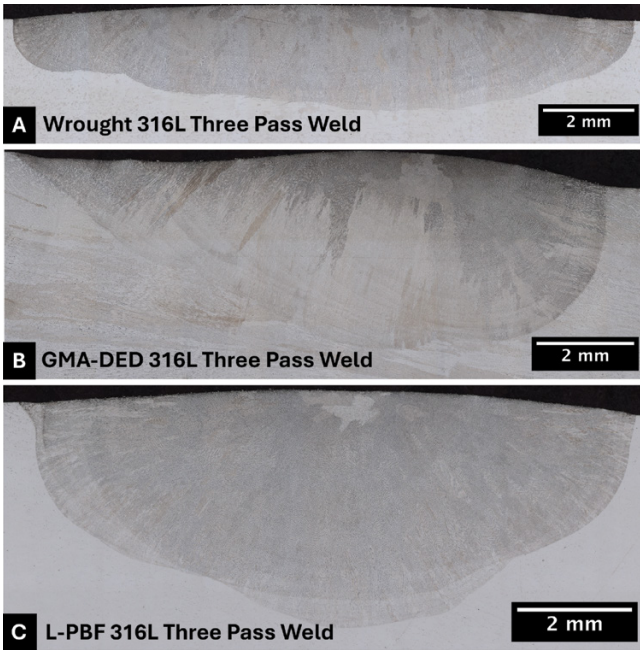


Fig. A4 —Three pass GTAW weld overview of: A — Wrought 316L; B — GMA-DED 316L; C — L-PBF 316L.

OLIVIA DENONNO and **JONAH KLEMM-TOOLE** (*jklemmto@mines.edu*) are with the Colorado School of Mines, Golden, Colo. **ROBERT HAMLIN** is with Naval Nuclear Laboratory, Niskayuna, N.Y. **STEPHEN TATE** is with the Electrical Power Research Institute, Charlotte, N.C.